An Effective Water Depth Correction for Pressure-Based Wave Statistics on Rough Bathymetry

OLAVO B. MARQUES,[a,b] FALK FEDDERSEN,[a] AND JAMES MACMAHAN[b]

[a] *Scripps Institution of Oceanography, University of California, San Diego, San Diego, California*
[b] *Oceanography Department, Naval Postgraduate School, Monterey, California*

(Manuscript received 8 September 2023, in final form 6 August 2024, accepted 26 August 2024)

ABSTRACT: Near-bottom pressure sensors are widely used to measure surface gravity waves. Pressure spectra are usually converted to sea surface elevation spectra with a linear-theory transfer function assuming constant depth. This methodology has been validated over smooth sandy beaches but not over complex bathymetry of coral or rocky environments. Bottom-mounted pressure sensors collocated with wave buoys in 10–13-m water depth from a 5-week rocky shoreline experiment are used to quantify the error of pressure-based surface gravity wave statistics and develop correction methods. The rough bathymetry has $O(1)$ m vertical variability on $O(1–10)$ m horizontal scales, much shorter than the 90–40-m wavelength of sea band (0.1–0.2 Hz). For sensor stability, pressure sensors were deployed by divers in bathymetric lows. When using the local depth measured by the pressure sensor, significant wave height squared overestimates the direct wave buoy measurements (up to 21%) in the sea band. An effective depth hypothesis is proposed where a spatially averaged water depth provides more accurate wave height statistics than the local depth at the pressure sensor. An optimal depth correction, estimated by minimizing the wave height error, varies from 0.1 to 1.6 m. A bathymetry averaging scale of 13 m is found by minimizing the median bathymetry deviation relative to the optimal. The optimal and averaged bathymetry depth corrections are similar across locations and, using linear theory, significantly reduce wave statistical errors. Therefore, pressure-based wave measurements require a correction that depends on the spatially averaged bathymetry around the instrument. The larger errors when using the local depth suggest that approximately linear surface waves are not strongly modified by abrupt depth changes over $O(1)$ m horizontal scales.

SIGNIFICANCE STATEMENT: The measurement of surface waves by bottom-mounted pressure sensors relies on wave theory formally derived for constant depth. We show that the constant depth assumption leads to systematic errors in wave statistics from observations over a rough, rocky bottom. By considering a spatially averaged bathymetry instead of the local water depth at the pressure sensor, the accuracy of wave energy density is improved, and upper-bound biases decay from 20% to 10%.

KEYWORDS: Gravity waves; Oceanic waves; Pressure; In situ oceanic observations

1. Introduction

Pressure sensors are routinely used to describe surface gravity wave statistics such as wave spectra, significant wave height, and wave energy flux and are fundamental to observations of wave transformation in the nearshore. Cross-shore arrays of pressure sensors provide gradients in sea-swell wave statistics associated with wave shoaling and dissipation on sandy shore environments (e.g., Thornton and Guza 1982, 1983; Raubenheimer et al. 1996; Herbers et al. 1999), coral reef environments (e.g., Lowe et al. 2005; Monismith et al. 2015; Lentz et al. 2016; Rogers et al. 2016; Acevedo-Ramirez et al. 2021; Sous et al. 2023), and rocky shores (Farrell et al. 2009; Poate et al. 2018; Gon et al. 2020; Lavaud et al. 2022). The energetics of surface gravity waves are important for driving several processes in the nearshore, such as the circulation (e.g., MacMahan et al. 2006), infragravity waves (e.g., Bertin et al. 2018), runup at the shoreline (e.g., Gomes da Silva et al. 2020), sediment transport on sandy beaches (e.g., Elfrink and Baldock 2002), and dispersal of tracers (e.g., Moulton et al. 2023). Accurate estimates of surface gravity wave statistics from pressure sensors are crucial for measuring how waves transform, drive currents, and induce mixing between the surfzone and inner shelf.

Surface gravity wave statistics are typically estimated from pressure measurements using linear wave theory and assuming constant water depth h. A transfer function K converts the observed pressure spectrum [$S_p(f)$, where f is frequency] to a surface elevation spectrum [$S_\eta(f)$], i.e.,

$$S_\eta(f) = K^2 S_p(f), \tag{1}$$

where K is given by (e.g., Dean and Dalrymple 1991)

$$K = \frac{\cosh(kh)}{\cosh(kz_{\text{hab}})}, \tag{2}$$

where z_{hab} is the height above the bottom for the pressure measurement and k is the radian wavenumber derived from the linear-theory dispersion relationship:

$$\omega^2 = gk\tanh(kh), \tag{3}$$

where ω is the radian wave frequency ($\omega = 2\pi f$) and g is the gravitational acceleration. In practice, the water depth h is

Corresponding author: Olavo B. Marques, omarques@ucsd.edu

DOI: 10.1175/JTECH-D-23-0118.1

estimated from the mean pressure and knowing z_{hab}. In many nearshore applications, pressure sensors are deployed near the bed. Thus, z_{hab} is often small (1–10 cm) and $\cosh(kz_{hab}) \approx 1$. Similar transfer functions can be derived for constant depth from linear theory to relate horizontal and vertical velocity spectra to S_η (Herbers et al. 1992).

A well-known issue with this transformation is that K grows exponentially at large kh so that pressure noise becomes amplified, and typically, a high-frequency cutoff is applied to avoid contamination of wave statistics (e.g., Raubenheimer et al. 1996). Validation of pressure-based wave height statistics from (1) to (3) against statistics from direct measurements of the surface elevation in the laboratory (Bishop and Donelan 1987) and in the field (Guza and Thornton 1980) reported an accuracy within 10%, where the validation was performed over $0.1 < kh < 2$, with small enough K^2 to prevent noise amplification. A few comparisons have been obtained between directly measured $S_\eta(f)$ and K^2S_p on the inner shelf. In a low-sloped sandy bay, collocated Spotter (GPS-based) wave buoy and pressure sensor integrated within an acoustic Doppler current profiler (ADCP) in $h \approx 7$ m have a good time-mean spectral comparison in the sea–swell (0.05–0.2 Hz) band (Lancaster et al. 2021). Offshore of a low-sloped sandy beach in $h \approx 10$ m, a comparison between a pressure sensor and an acoustic surface tracker on an ADCP showed that linear theory accurately estimated S_η out to at least $kh \approx 1.5$ (Martins et al. 2021). Recently, a comparison of various wave buoys and a pressure-sensor array in 8-m water depth showed that the wave buoys were consistent with the linear-theory-transformed pressure measurements across the 0.07–0.25-Hz band (Collins et al. 2024). The linear-theory transfer function (2) is derived under a constant h approximation. For smooth and weak bathymetric slope (i.e., bathymetry varying on scales longer than a wavelength), this assumption works well both seaward of the surfzone (e.g., Herbers et al. 1992; Collins et al. 2024) where bathymetric slopes are typically <0.01 and through the surfzone (e.g., Thornton and Guza 1983; Herbers et al. 1999) where bathymetric slopes are generally < 0.04.

Wave nonlinearity is not incorporated in (1)–(3), and increasingly nonlinear waves modify the relationship between near-bed pressure and sea surface elevation. A weakly nonlinear and weakly dispersive (small kh) method can reproduce the sea surface of a soliton from bottom pressure (Bonneton and Lannes 2017) and wave time series for just offshore of the surfzone (Bonneton et al. 2018). For $O(1)$ kh where triads are not resonant, the relationship between S_η and S_p can change as a certain fraction of the wave energy at a particular frequency is bound (e.g., Hasselmann 1962). However, in ≈7-m depth, the fraction of bound energy at $f < 0.2$ Hz is generally small even for large waves (Herbers et al. 1992), and the relationship between pressure and velocity is well predicted by linear wave theory (Herbers et al. 1992). This relationship is so consistent even within the surfzone that it is used as a method of quality controlling current meter data (Elgar et al. 2001). For weakly dispersive waves, large waves can also change the dispersion relationship through amplitude dispersion which was detectable in the field (Herbers et al. 2002) and laboratory (Martins et al. 2021). Linear theory also neglects the velocity-squared terms in the Bernoulli equation, which can be significant for estimating wave setdown and setup (Raubenheimer et al. 2001). However, for realistic conditions, this term contributes 2.5-cm root-mean-square to hydrostatic pressure (Lentz and Raubenheimer 1999) and is thus generally negligible for estimating wave properties.

In contrast with sandy beaches, coral reefs and rocky shores support large multiscale bathymetric variability at scales much shorter than the sea–swell wavelengths (i.e., large slopes and slope variability), and the constant h assumption in (1)–(3) is questionable. For example, coral reef bathymetry has steep fore reefs, gently sloping flat reefs, and spur-and-groove formations, all of which can have $O(1)$ m depth changes over $O(1)$ m horizontal distance (e.g., Monismith 2007; Davis et al. 2021), scales much shorter than the $O(10–100)$-m wavelength of sea–swell waves. Despite complex bathymetry, wave statistics are often estimated by applying linear wave theory to pressure sensor data, taking h as the depth calculated from the data (e.g., Monismith et al. 2015). Similarly, wave height estimates from pressure sensors have also been made over rocky bathymetry, which may have $O(1)$ m variability in h over horizontal scales much shorter than sea-swell wavelengths (Farrell et al. 2009; Poate et al. 2018; Gon et al. 2020; Lavaud et al. 2022). No validation of pressure-derived wave statistics has been performed on coral reefs or rocky shores.

Assuming a constant h approximation with (2)–(3) can be used in rough complex bathymetric regions to derive wave statistics, it is unclear that the local pressure-sensor-estimated h is the appropriate choice. For wavelengths and water depths with small kh (e.g., Lentz et al. 2016), waves are largely hydrostatic, K is approximately 1 throughout the water column, and the choice of h may not be important. However, in regions with $O(1)$ kh and rough bathymetry, the transfer function is likely sensitive to the depth, which would affect wave statistics. Accurate surface gravity wave statistics are particularly important for spatial instrument arrays where gradients of wave statistics are taken across horizontal scales of $O(10–100)$ m. Gradients of wave energy flux derived from pressure sensors show larger wave bottom friction dissipation over coral reefs or rocky shores than on sandy beaches (e.g., Lowe et al. 2005; Gon et al. 2020). Large bottom friction dissipation has been observed (Lowe et al. 2005; Gon et al. 2020) at large water depth, where depth-limited wave breaking is negligible, but errors in K for large kh could be significant. Therefore, if the constant depth assumption underlying (1)–(3) leads to substantial errors in the surface elevation spectrum, the contamination not only extends to wave height and energy flux but also extends to wave dissipation estimates across the array.

Here, we use bottom-mounted pressure sensors with collocated wave buoys to address the accuracy of linear wave theory to estimate wave heights from pressure data over complex and rough bathymetry in approximately 10-m water depth. Observations are from a 5-week experiment that was carried out in the Monterey Peninsula (California, United States) as part of the Rocky Shores Experiment and Simulations (ROXSI). The instrument array and bathymetry are described in section 2. The accuracy of linear wave theory in (1)–(3) using the local

water depth on highly variable rough bathymetry is tested in section 3. In section 4, we propose and test an effective depth hypothesis, where the depth from a spatially averaged bathymetry results in more accurate wave statistics than the local depth from a pressure sensor. Comparisons with a sandy inner shelf, application to other environments with complex bathymetry (e.g., coral reefs), and the implications of the effective depth are discussed in section 5. A summary is presented in section 6.

2. Methods

a. *Field site and bathymetry*

The first ROXSI field experiment was carried out off China Rock, Pebble Beach, California, United States, during June–July 2022 (Fig. 1). The goal of ROXSI is to study how rough rocky bathymetry impacts waves and circulation in the nearshore. The shoreline at China Rock (Fig. 1a) and most of the bathymetry (Fig. 1b) are composed of large rocks.

Multiple datasets were combined to map the bathymetry as, in contrast to sandy shores, rocky morphology only changes on geological time scales. Multibeam bathymetry gridded at 2-m resolution for water depths greater than ≈10 m is available from the California State University, Monterey Bay (CSUMB, Seafloor Mapping Laboratory 2014). The uncertainty on the vertical elevation of the multibeam bathymetry is ±5 cm^{-1} (Barnard et al. 2011). Shallower bathymetry was measured with a bathymetric lidar by the Joint Airborne Lidar Bathymetry Technical Center of Expertise (JALBTCX). The JALBTCX dataset covers most of the study site, and the data distribution is irregular with a varying resolution between 0.5 and 2 m, with individual point error of ~15 cm (OCM Partners 2024). A small fraction of our bathymetry data were also obtained from a surveying system mounted on a Rotinor DiveJet underwater scooter. Flotation was added to the DiveJet, which is operated at the surface by one person. A frame was mounted in front of the DiveJet to hold a survey-grade GPS above a downward-looking Nortek Signature 1000 ADCP. The ADCP has an echosounder that was programmed to sample at 4 Hz. Bottom-depth data at locations where different datasets overlap are consistent with each other. Finally, subaerial topography is available from the National Oceanic and Atmospheric Administration (NOAA). Elevations relative to mean sea level z from the combined datasets were gridded to 2-m horizontal resolution (Fig. 1b).

The shoreline and bathymetry at China Rock have variability at a wide range of scales (Fig. 1). On horizontal scales of hundreds of meters, the shoreline has small headlands and embayments spaced by 100–200 m. The bathymetry has a moderate (1:40) cross-shore slope. Rocky formations lead to large seafloor roughness on vertical scales of O(1–10) m (Fig. 1c). For example, the standard deviation of z within 5-by-5-m squares has a median of 0.5 m across the study site. The difference between the maximum and the minimum in each square, which is a better representation of the height of larger rocks, has a median of 2 m (consistent with the photo in Fig. 1a and the perturbation depth in Fig. 1c). In addition to areas with large bottom roughness, rock aggregates are

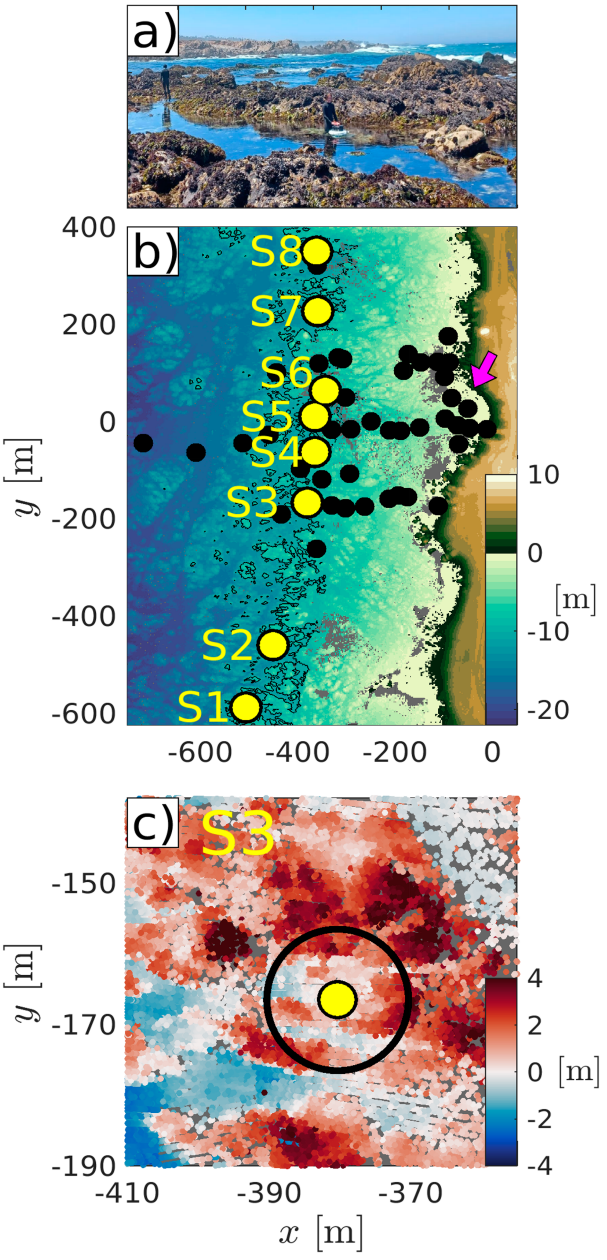

FIG. 1. (a) Image of the China Rock (Pebble Beach, California, United States) shoreline taken at low tide, where rocks can be a few meters tall. (b) Instrument array (circles) over the rough rocky bathymetry off China Rock. An array of eight Smart Moorings (yellow dots), collocated wave buoys, and pressure sensors was deployed at a depth of ≈10 m. We denote the Smart Mooring locations as S1–S8 going from south to north. Colors in (b) show the 2-m gridded elevation relative to mean sea level elevation with the 10-m isobaths contoured. The location from where the photo in (a) was taken is denoted by the magenta arrow in (b). (c) Ungridded perturbation depth relative to the depth of the S3 pressure sensor [i.e., $-(h-\overline{h}_p)$], where positive (red) and negative (blue) indicate shallower and deeper depths than at the pressure sensor (yellow), respectively. The black circle in (c) indicates a distance of 10 m from the S3 location. Maps in (b) and (c) are shown in a local cross-shore and alongshore (x, y) coordinate system, where $-x$ is offshore and directed to 285°N.

mingled with patches of sand, where the bathymetry is smoother (e.g., around $x = -600$ m and $y = 0$ m in Fig. 1b).

b. Instruments and data processing

Our analysis will focus on collocated observations of sea surface elevation and near-bottom pressure from an alongshore array around the 10-m isobath of eight SOFAR Smart Moorings (yellow circles in Fig. 1). These measurements are part of a 54-instrument array deployed from 15 June to 21 July 2022 to measure wave transformation over the rocky bathymetry off China Rock (black and yellow circles in Fig. 1b). Instruments measuring surface gravity waves included SOFAR Spotter wave buoys (Herbers et al. 2012; Raghukumar et al. 2019), Nortek ADCPs, and bottom-mounted RBR Coda and SoloD pressure sensors.

The deployed SOFAR Smart Mooring system combined a bottom-mounted RBR Coda pressure sensor cabled to a Spotter wave buoy. The Spotter is a GPS-based wave buoy, as opposed to a pitch-and-roll-based wave buoy (Herbers et al. 2012; Raghukumar et al. 2019; Beckman and Long 2022). Three-dimensional surface displacements are provided by the Spotter at a sampling rate of 2.5 Hz, and the manufacturer quoted uncertainty of the vertical elevation is 2 cm (Sofar Ocean 2024). For frequencies higher than 0.06 Hz, field observations show good agreement between sea–swell wave statistics from Spotter measurements and pressure sensors (Collins et al. 2024) or pitch-and-roll-based wave buoys (Herbers et al. 2012; Raghukumar et al. 2019; Beckman and Long 2022). In particular, mean significant wave heights from the Spotter are within ≈4% from other instruments, and the relative root-mean-square error is less than or equal to 6 cm (Collins et al. 2024). Time series duration from the eight Smart Moorings varied from 24.5 to 32 days (588–768 hourly estimates of significant wave height).

The pressure sensors collocated with Spotter buoys in the Smart Mooring sampled at 2 Hz and were deployed in bathymetric lows on weighted plates at a height above the local rough rocky bathymetry $z_{\mathrm{hab}} = 0.13$ m. Given the large bottom roughness, the water depth in a pressure sensor's vicinity (i.e., at 10 m horizontal scale) can be a few meters shallower (Fig. 1c). Pressure in units of pascal is converted to units of meters by normalization with $\rho_0 g$, where $\rho_0 = 1025$ kg m^{-3} and $g = 9.8$ m s^{-2}. Hourly averaged atmospheric pressure P_{atm} was measured at a NOAA pressure gauge in the Monterey Harbor (≈6 km from our site). A 3-cm offset was subtracted from P_{atm} based on a comparison to our pressure sensors when exposed in the intertidal zone. The hourly averaged water depth h_p is given by

$$h_p = \frac{P - P_{\mathrm{atm}}}{\rho_0 g} + z_{\mathrm{hab}}, \tag{4}$$

where P is the hourly averaged pressure p.

Hourly pressure spectra S_p were computed using 120-s-long segments (frequency resolution ≈0.008 Hz) that were tapered with a Hann window and with 50% overlap yielding 118 degrees of freedom. Surface elevation wave spectra S_η from the Spotter were similarly computed. The standard approach to compute S_η from S_p is to use the local depth h_p to calculate wavenumbers k through the linear dispersion relationship in (3) and the transfer function K in (2). This approach assumes constant depth. The significant wave height can then be computed from either Spotter H_{sp} or pressure H_p measurements as

$$H \equiv 4\sqrt{\int S_\eta df}\,. \tag{5}$$

Throughout this paper, we compute significant wave height H in the sea band between 0.1 and 0.2 Hz. For the range in time-mean water depths at instrument locations ($9.7 < \overline{h}_p < 13.6$ m), the frequency range where H is computed corresponds to wavelengths between 36 and 105 m and kh between 0.7 and 2.2. The $0.1 < f < 0.2$ Hz frequency band includes the surface wave peak periods for most of the experiment and has negligible contamination from pressure noise amplified by K^2 at high frequencies. Based on a S_p noise floor of 5×10^{-6} m^2 Hz^{-1} (i.e., with an equivalent 0.2 cm uncertainty) and a water depth of 13.6 m, the significance level of H_p is less than 1 cm. For an upper integration limit of 0.3 Hz, the significance level increases to 8 cm, which is larger than the expected errors in the Spotter significant wave height (Collins et al. 2024). Biases in H_p were estimated at up to 1 cm based on measurements from collocated pressure sensors in h_p from 7 to 13 m for a separate deployment at the China Rock site in similar wave conditions.

3. Accuracy of transfer function using h_p

Although the pressure-based estimate of water depth h_p yields accurate H_p over low-sloped sandy beaches (e.g., Guza and Thornton 1980), the rocky bathymetry at our site has large vertical variability on horizontal scales of O(1–10) m, which are shorter than the wavelength of sea and swell surface gravity waves (Fig. 1c). Thus, it is unclear whether h_p leads to reliable estimates of H_p. Since the Smart Moorings provide collocated pressure and surface elevation measurements, we can assess the accuracy H_p.

At the eight Smart Mooring locations, the Spotter significant wave height H_{sp} varied from 0.2 to 2 m (corresponding to a range of H_{sp}^2 between 0.04 and 4 m^2; Fig. 2) largely on synoptic and diurnal time scales. Here, we focus on H^2 as it directly relates to wave energy. Along the array, the time-mean H_{sp}^2 varied between 0.65 and 0.81 m^2, with no consistent alongshore pattern. The observed H_p^2 (using h_p) is in overall reasonable agreement with H_{sp}^2, but H_p^2 is biased high at most locations (Fig. 2).

The accuracy of H_p^2 relative to H_{sp}^2 is quantified with the correlation coefficient, the linear regression slope, and the mean-square error:

$$\epsilon_0^2 = \overline{(H_p - H_{\mathrm{sp}})^2}, \tag{6}$$

where $\overline{(\ldots)}$ is a time average over the individual instrument deployment, varying between 588 and 768 hourly data points across different instruments. The squared error metric ϵ_0^2 is convenient because it is proportional to wave energy and

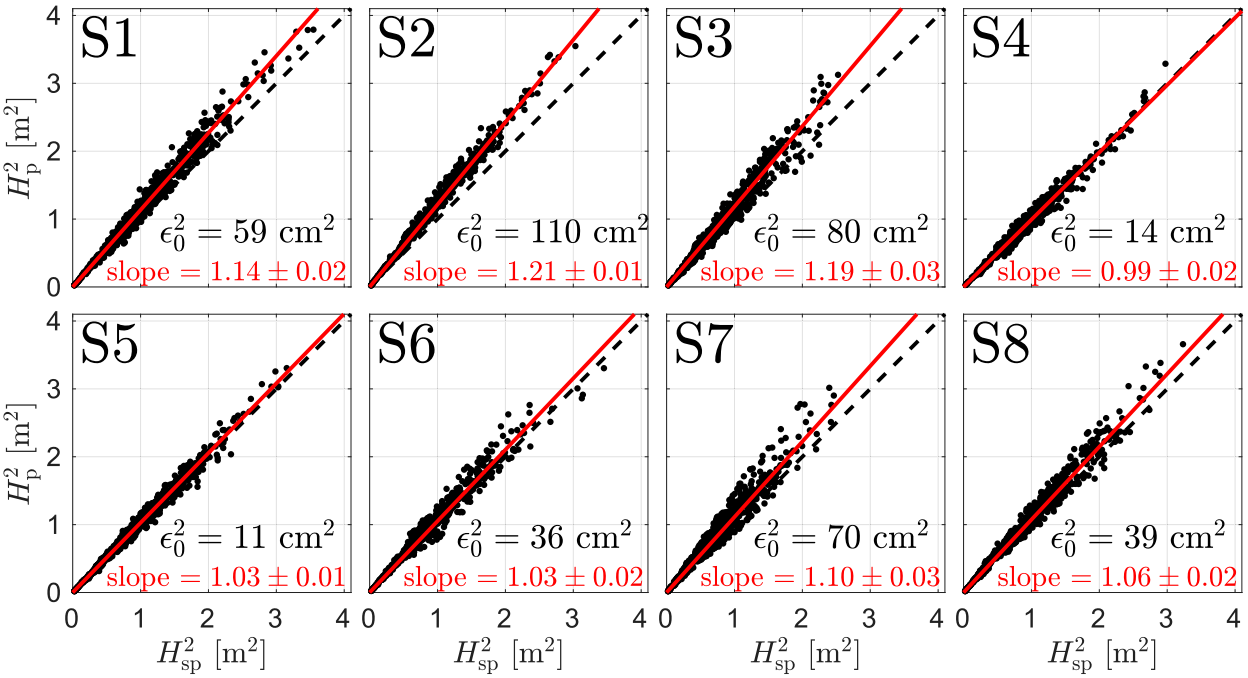

FIG. 2. Collocated hourly pressure-based H_p^2 vs Spotter wave-buoy-based H_{sp}^2 significant wave height squared at the eight Smart Mooring locations (Fig. 1b). The mean-square error from (6) and regression slope with its 95% confidence limit are shown at each location. The black dashed line is the one-to-one line. From the regression slopes, H_p^2 consistently overestimates H_{sp}^2.

allows straightforward comparison to studies examining errors in significant wave height from wave buoy data (Raghukumar et al. 2019; Lancaster et al. 2021; Beckman and Long 2022; Collins et al. 2024). Both bias and random noise affect ϵ_0^2.

Along the array, H_p^2 is consistently biased high relative to H_{sp}^2 (Fig. 2), even though the squared correlation between the two is high at all locations ($r^2 > 0.94$, not shown). The regression slopes vary from 1.21 at S2 to 0.99 at S4 with an average of 1.09. The southernmost locations have the highest slopes. The regression slope is significantly above unity at seven out of eight locations, whereas the underestimate at S4 is statistically insignificant. Larger ϵ_0^2 is primarily associated with larger regression slopes (e.g., S2).

We next compare the time average (over the experiment duration) of the Spotter wave spectra $\overline{S}_\eta$ to the pressure-sensor wave spectra $\overline{K^2(h_p)S_p}$ at location S3 (Fig. 3). This location has large H_p^2 overestimates relative to H_{sp}^2 (Fig. 2), but does not have the largest error. We use this location throughout as an example of how errors in H_p^2 will be addressed. The mismatch between $\overline{K^2 S_p}$ and $\overline{S}_\eta$ is frequency dependent. In the swell band ($f < 0.1$ Hz), the two spectra are largely similar as kh is relatively small and $K^2 \leq 1.6$. However, in the sea band ($0.1 < f < 0.2$ Hz), $\overline{K^2(h_p)S_p}$ is consistently elevated over $\overline{S}_\eta$, where the ratio between their sea-band-integrated spectra is 1.17. Therefore, the overestimated H_p is due to errors at relatively large kh in the sea-band waves (and not swell), because the sea band at our instrument sites has $kh > 0.7$ and rapidly growing K^2 from 1.6 to 8.3 between 0.1 and 0.2 Hz. The errors in the sea band observed at S3 are qualitatively similar across all Smart Mooring locations. The overestimated H_p^2 and $K^2 S_p$ will lead to overestimated wave energy, wave energy fluxes, and radiation stress, which all depend on the sea surface elevation spectrum. We next explore the cause of the bias between the pressure sensor and Spotter and how to correct the bias.

4. Correction of wave height estimates over complex bathymetry

On the one hand, the form of the linear wave theory transfer function (2), derived for a flat bottom, is supported by the high correlation between H_p from pressure sensors and H_{sp} from Spotter wave buoys (Fig. 2). On the other hand, H_p systematically overpredicts H_{sp} suggesting that the transfer function requires modification. If $K(h_p)$ were an accurate transfer function, this would suggest that surface waves adjust rapidly over short horizontal distances to sharp bathymetric changes (Fig. 1c), contradicting linear theory. However, if surface gravity waves are instead only responding to water depth changes at some longer spatial scales, then simply an appropriate effective water depth h_{eff}, different than h_p, can be used within linear theory.

Our hypothesis, denoted the effective depth hypothesis, is that wave statistics can be corrected by replacing h_p with an effective depth h_{eff} calculated from the mean h around an instrument site (Fig. 4). For sensors deployed in bathymetric lows, $h_{eff} < h_p$ which leads to $K(h_{eff}) < K(h_p)$, thereby reducing the overestimation in $K^2 S_p$ and H_p^2. Therefore, using h_{eff} instead of h_p could reduce the observed H_p^2 and time-mean

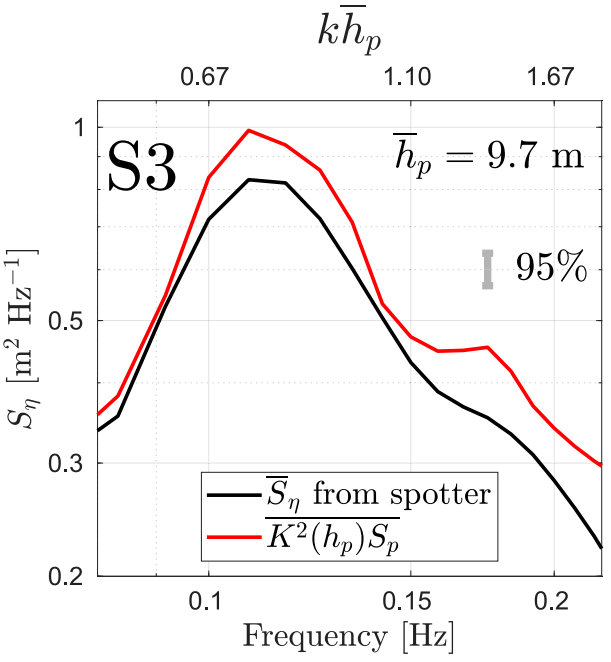

FIG. 3. Time-averaged Spotter sea surface elevation spectra $\overline{S}_\eta$ (black) and pressure-sensor estimated $\overline{K^2 S_p}$ vs frequency at location S3. The time-averaged pressure-sensor-measured depth is $\overline{h}_p = 9.7$ m. The top axis shows nondimensional $k\overline{h}_p$ corresponding to the frequency axis and $\overline{h}_p$ using the linear dispersion relationship (3). The 95% error bound for the time-averaged spectra (with 2268 degrees of freedom) is shown in the upper right.

spectra errors. As an example, the time-mean transfer function K^2 at location S3 decreases when reducing the water depth by 1 m (Fig. 4b), which is a reasonable vertical scale based on the bathymetry around location S3 (Fig. 1c). Although the hourly water depths and the correspondent wavenumbers are changed by a constant, the difference in K^2 is a function of frequency, with larger changes toward higher frequencies (and kh).

However, it is unclear a priori what the relevant spatial scale for averaging the bathymetry is and how to calculate a depth correction δh such that $h_{\text{eff}} = h_p + \delta h$. Using the bathymetry and collocated measurements of pressure and sea surface elevation from the Smart Mooring array, the effective depth hypothesis can be tested. We first calculate an effective depth correction using only the wave observations and then compare it to bathymetry averaged at different spatial scales. We consider a depth correction for the significant wave height, and thus, the calculated depth corrections do not depend on wave frequency.

a. *Effective depth from observations*

To determine an optimal water depth correction δh_{opt}, we find the depth correction that minimizes the error between H_p and H_{sp}. The error $\epsilon^2(\delta h)$ is defined similar to (6):

$$\epsilon^2(\delta h) = \overline{[H_p(h_p + \delta h) - H_{\text{sp}}]^2}, \tag{7}$$

where $H_p(h_p + \delta h)$ is based on $K^2(h_p + \delta h)S_p$ integrated between 0.1 and 0.2 Hz, and the depth change also modifies the estimated wavenumbers k in the linear dispersion relationship (3). At each location, we compute $\epsilon^2(\delta h)$ where δh is varied from −3 to 0 m at 0.1-m intervals. The optimal water depth correction δh_{opt} equals δh that minimizes (7). Posterior estimates on the uncertainty of δh_{opt} are estimated assuming $[\epsilon^2(\delta h) - \epsilon^2(\delta h_{\text{opt}})]/\epsilon^2(\delta h_{\text{opt}})$ is a Gaussian random variable.

For example, $\epsilon^2(\delta h)$ at location S3 is shown in Fig. 5. For no depth correction ($\delta h = 0$), $\epsilon^2(\delta h)$ is equivalent to $\epsilon_0^2 = 80\,\text{cm}^2$ (Fig. 2, S3). The error ϵ^2 is a parabola with δh, and the optimal $\delta h_{\text{opt}} = -1.5$ m minimizes $\epsilon^2(\delta h)$ to 20 cm^2 reducing the mean-square error to one quarter of ϵ_0^2. Negative δh_{opt} is consistent with pressure sensors deployed in bathymetric lows (Fig. 1c) and the effective depth hypothesis (Fig. 4), i.e., h_{eff} is shallower than h_p. At all locations, the $\epsilon^2(\delta h)$ curve is qualitatively similar, and δh_{opt} is always negative, varying from −1.6 to −0.1 m. Note that δh_{opt} is entirely based on the pressure and wave buoy observations and does not consider the bathymetry. Although we

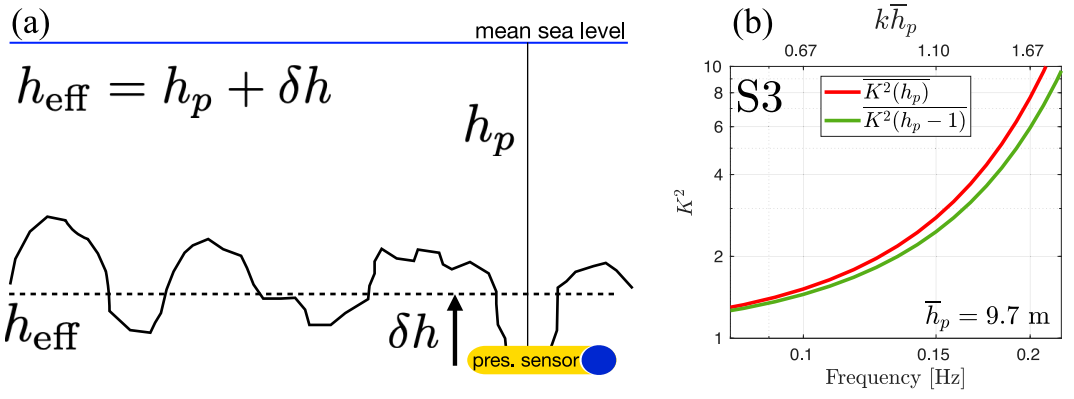

FIG. 4. (a) Schematic of the rough bathymetry with a pressure sensor in a bathymetric low. Water depth is defined as positive, where h_p is the local depth at the pressure sensor and the effective depth h_{eff} is a spatially averaged bathymetry. For a pressure sensor in a bathymetric low, $\delta h < 0$. (b) Time-mean transfer functions K^2 computed at the observed depth h_p at instrument site S3 (red) and at a shallower depth $h_p - 1$ m (green).

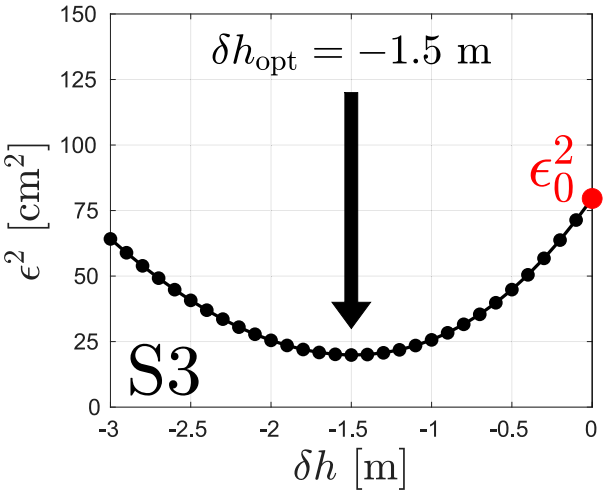

FIG. 5. Mean-square error ϵ^2 from (7) between H_p^2 and H_{sp}^2 vs δh at location S3. The minimum of ϵ^2 gives the best correction factor δh_{opt}.

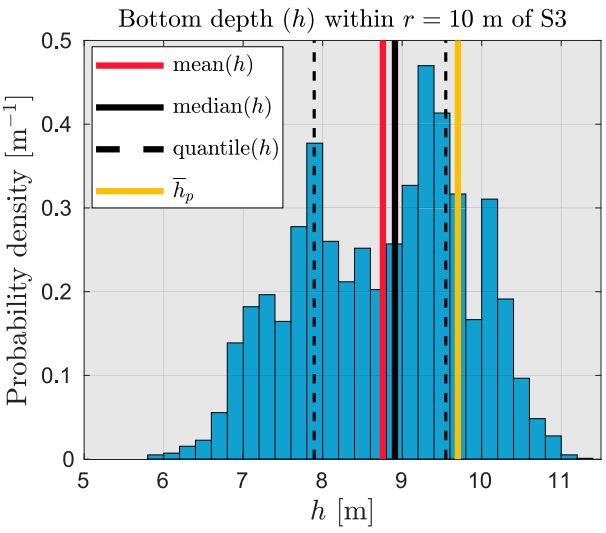

FIG. 6. Probability density function of water depths h within a circle with radius $r = 10$ m of instrument location S3 (circle in Fig. 1c) centered on the pressure sensor location. The mean depth (red), median depth (solid black), and 1/3 and the 2/3 quantiles (dashed black lines) are shown as is the time-mean pressure-sensor-estimated depth $\overline{h}_p$ (yellow).

find negative optimal depth correction at all locations, δh_{opt} alone does not inform what bathymetry averaging length scale is appropriate for computing h_{eff}.

b. *Effective depth from bathymetry*

Since we have the bathymetry around the Smart Mooring array, the ungridded bathymetry point cloud is averaged over different radii length scales to find the length scale yielding a depth correction most consistent with δh_{opt}. The density of bathymetric data points within the region of the Smart Mooring array varies between 1 and 6 points per square meter. We first quantify the rough rocky bathymetry depth statistics near the pressure sensor at S3 (Fig. 1c) from the ungridded bathymetry with its probability density function (pdf; Fig. 6). Within a radius of 10 m (the nominal water depth), large depth variability occurs with maximum–minimum range of 5 m, and the 1/3–2/3 quantile range is 1.7 m (Fig. 6). The pressure-sensor-measured time-averaged depth $\overline{h}_p = 9.7$ m is toward the deeper tail of the pdf, deeper than the mean and median depths of ≈8.9 m (a difference of 0.8 m), and consistent with the pressure sensor located in a bathymetric low. The pdf of h around S3 yields a skewness of approximately −0.2, and the bathymetry around all Smart Mooring locations has negative skewness. The sign of the skewness of h is consistent with bathymetric lows that are slightly broader than shallower depth anomalies.

We compute depth statistics for radii between $2 \le r \le 30$ m at 1-m intervals to find an appropriate horizontal averaging scale to estimate h_{eff} (Fig. 7). At every r, the depth correction is given by

$$\delta h(r) \equiv [h](r) - \overline{h}_p, \tag{8}$$

where $[h](r)$ is either the mean or median water depth within a distance r from the pressure sensor (e.g., circle with $r = 10$ m is shown in Fig. 1c). The measured depth difference $\delta h(r)$ between mean bathymetry and $\overline{h}_p$ is always negative and has large variability across instrument locations, and the magnitude tends to increase with r, which indicates that the averaged water depth tends to get shallower (Fig. 7a). The negative sign of $\delta h(r)$ is consistent with the deployment of pressure sensors in bathymetric lows. The standard deviation of water depth σ_h at the $r = 30$-m scale (Fig. 7b) varies between 1.2 and 1.8 m across instrument sites. As expected, the variability of δh and σ_h is roughly consistent across instrument locations, where δh tends to increase with bottom roughness as measured by σ_h. For example, S1 and S2 are instrument locations with both relatively large δh and σ_h, while S4 and S5 have smaller δh and σ_h (Fig. 7). At shorter distances ($r < 10$ m), locations with larger σ_h have both a larger magnitude of δh and a larger gradient with respect to r, which implies that the height of the bathymetric lows increases as the horizontal scale increases. At these instrument locations (S1, S2, S3, S7, and S8), the gradient of δh decreases at distances between $r = 4$ and 10 m. The gradient of the mean σ_h with respect to r decreases from short to longer distances. This curvature of σ_h with r is associated with bottom slope variability that is larger at small scales than a relatively smoother bathymetry at longer spatial scales.

In general, each location has an optimal averaging scale resulting in a r and a δh that match δh_{opt}. For a simple depth correction that can be applied to any sensor, a single length scale was determined by minimizing the depth correction error, i.e.,

$$\mathcal{E}^2(r) = \langle (\delta h(r) - \delta h_{\text{opt}})^2 \rangle, \tag{9}$$

where $\langle \cdot \rangle$ is an average across all eight Smart Mooring locations. Averaging over all instrument sites, at similar water depths, increases statistical reliability in determining an optimal $\hat{r}$, which corresponds to the scale where $\mathcal{E}^2$ has a minimum.

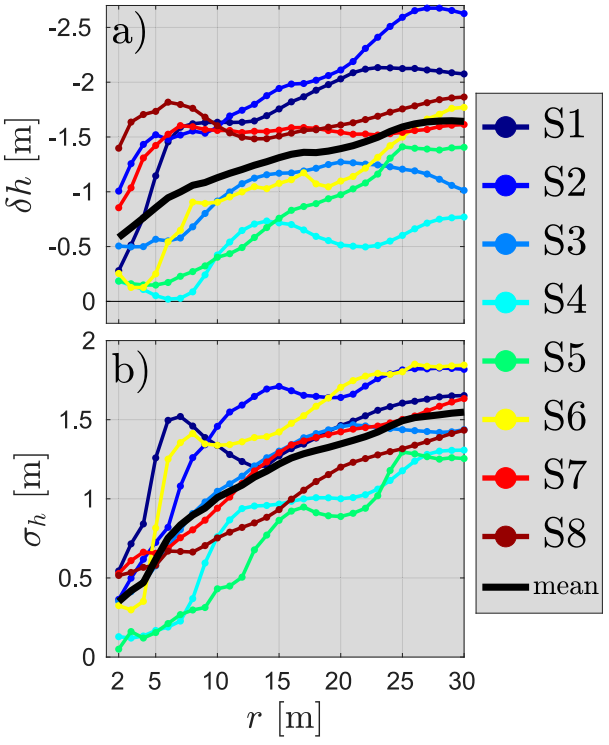

FIG. 7. (a) Bathymetric correction $\delta h(r)$ in (8), given by the difference between the mean water depth within a distance r from the instrument location and the time-mean observed water depth $\overline{h}_p$. (b) The standard deviation of water depth σ_h within a distance r from the instrument location. The mean (black line) in (a) and (b) is the average across all instrument locations (colored lines). The correction $\delta h(r)$ from median water depth is similar to (a).

The mean-square errors $\mathcal{E}^2$ have well-defined global minima at $\hat{r} = 11 \pm 3$ m for the mean and $\hat{r} = 13 \pm 3$ m for the median (Fig. 8), where the uncertainties of $\hat{r}$ are estimated assuming $[\mathcal{E}^2(r) - \mathcal{E}^2(\hat{r})]/\mathcal{E}^2(\hat{r})$ is a Gaussian random variable. The median at $\hat{r} = 13$ m has $\mathcal{E}^2$ that is 25% reduced from the mean at $\hat{r} = 11$ m, suggesting that the median bathymetry at $\hat{r} = 13$ m is an appropriate water depth to evaluate the transfer functions (2). We calculate δh_{bathy} at all locations using the median bathymetry at $\hat{r} = 13$ m. As expected, all locations have $\delta h_{\text{bathy}} < 0$, indicating that pressure sensors were in relative bathymetric lows. Five locations (S1, S2, S3, S7, and S8) had rougher bathymetry and deeper bathymetric lows $-1.5 \le \delta h_{\text{bathy}} \le -1$ m, whereas $\delta h_{\text{bathy}} > -0.7$ m indicates a smoother bottom at the other three locations (S4, S5, and S6). The larger magnitude of depth corrections over rougher topography is also indicated by the correlation between $-\delta h_{\text{opt}}$ ($-\delta h_{\text{bathy}}$) and σ_h, calculated within $\hat{r} = 13$ m, where the correlation coefficient is $r = 0.7$ ($r = 0.5$).

c. *Accuracy of transfer function at h_{eff}*

The bathymetric corrections δh_{bathy} using a single averaging scale $\hat{r} = 13$ m are consistent with δh_{opt} (Fig. 9). In terms of magnitude, the corrections qualitatively have two groupings. The first grouping (S4, S5, and S6) has smaller ($\le$0.7 m) depth

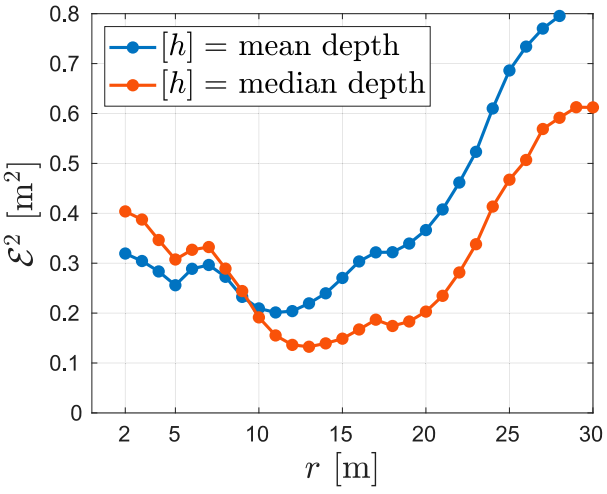

FIG. 8. Bathymetric correction error $\mathcal{E}^2$ from (9) averaged across all instrument locations (S1–S8) vs r based on mean (blue) and median (orange) water depths.

corrections δh_{bathy}, whereas the second grouping (S1, S2, S3, S7, and S8) has larger 1–1.5-m corrections (Fig. 9). These two groupings are separated by the δh_{opt} error bars and the 1/3–2/3 bathymetric quantiles (vertical and horizontal bars in Fig. 9). The δh_{bathy} is roughly proportional to δh_{opt} with a near-one slope. Location S8 has the largest deviation from the one-to-one line with a 0.8-m difference between δh_{opt} and δh_{bathy} (Fig. 9). Further deviations from the 1:1 relationship might be due to the variability of higher-order bottom-depth statistics (e.g., skewness), but we did not consider a statistical model to predict δh_{opt} from δh_{bathy} from multiple statistical moments. Nevertheless, the overall similarity between δh_{opt} and δh_{bathy} supports the effective depth hypothesis.

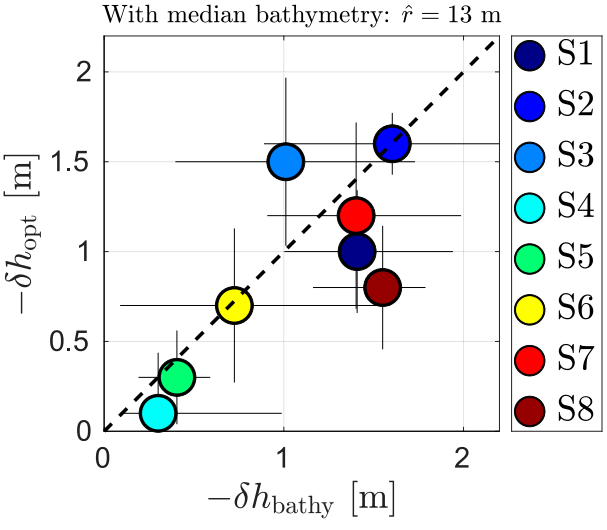

FIG. 9. Optimal depth correction $-\delta h_{\text{opt}}$ vs the depth correction $-\delta h_{\text{bathy}}$ from the median depth with $\hat{r} = 13$ m. The dashed line is the 1-to-1 line. The horizontal bars represent the 1/3–2/3 bathymetry quantile range. The vertical error bars represent the uncertainty in the δh_{opt} estimate.

We next explore how using a h_{eff} derived from either δh_{opt} or δh_{bathy} improves the significant wave height estimates at locations S3 and S4 (Fig. 10), chosen for their differing uncorrected H_p errors (Fig. 2) and contrasting δh (Fig. 9). The S3 uncorrected H_p^2 has large errors $\epsilon_0^2 = 80\,\text{cm}^2$ and a large regression slope of 1.19 (Fig. 10a). With the optimal correction using $\delta h_{\text{opt}} = -1.5$ m, H_p^2 more closely matches H_{sp}^2 (Fig. 10c) with best-fit slope near one and small $\epsilon^2 = 20\ \text{cm}^2$, a 75% error reduction relative to the uncorrected. Using δh_{bathy}, the corrected H_p^2 is also much closer to H_{sp}^2 than for the uncorrected (Fig. 10e). The corresponding $\epsilon^2 = 26\,\text{cm}^2$ is only slightly greater than that of δh_{opt}, and the best-fit slope is 1.08, a nearly 60% reduction in the bias. At location S4, the uncorrected depth h_p already yields small $\epsilon_0^2 = 14\,\text{cm}^2$, and thus, the optimal correction is very small $\delta h_{\text{opt}} = -0.1$ m with only marginally smaller ϵ^2. The bathymetric correction $\delta h_{\text{bathy}} = -0.3$ m has slightly larger magnitude than δh_{opt}, slightly increasing ϵ_0^2 (by 15%) and bias (by 5%) relative to uncorrected ($\delta h = 0$). Therefore, using either the bathymetrically averaged h_{eff} ($<h_p$) reduces H_p^2, and large overprediction of H_p can be significantly corrected (S3) while also not adding substantial error where δh_{bathy} is not far from δh_{opt} (S4).

We next examine the effect of the two depth corrections on the time-averaged wave spectra S_η at all eight locations (Fig. 11). As already seen for S3 (Fig. 3), the uncorrected $\overline{K^2(h_p)S_p}$ has small errors for $f \le 0.1$ Hz, but overpredicts the Spotter $\overline{S_\eta}$ within $0.1 < f < 0.2$ Hz at most locations (compare red and black curves; Fig. 11). Across the $0.1 < f < 0.2$-Hz band, the optimally corrected spectra $\overline{K^2(h_p + \delta h_{\text{opt}})S_p}$ is similar to the Spotter $\overline{S_\eta}$ (compare black to green curves; Fig. 11). The bathymetric correction δh_{bathy}, using $\hat{r} = 13$ m at all locations, yields time-mean spectra closer to the Spotter-based spectra than estimates using the observed depth h_p, particularly for moderate and large ϵ_0^2 (compare blue and black curves; Fig. 11). At lower frequencies $f < 0.1$ Hz, the spectra using h_p or the optimal or bathymetric depth corrections result in similar time-mean spectra, because kh is relatively small (<0.82), resulting in small changes to K^2.

In general, the depth correction has variable frequency-dependent accuracy (Figs. 11 and 12). For example, the $\overline{K^2(h_p + \delta h_{\text{bathy}})S_p}$ spectrum at location S2 has the best agreement with both $\overline{S_\eta}$ and $\overline{K^2(h_p + \delta h_{\text{opt}})S_p}$, and the error is very small across frequencies. For location S3, $\overline{K^2(h_p + \delta h_{\text{bathy}})S_p}$ overpredicts the spectrum at the peak frequency and is closer to $\overline{S_\eta}$ at higher frequencies. Errors in spectra corrected by δh_{opt} or δh_{bathy} are largely between $\pm 0.05\ \text{m}^2\ \text{Hz}^{-1}$ and are smaller than the errors in $\overline{K^2(h_p)S_p}$, implying the errors after applying the depth corrections are primarily random (Figs. 12b,c). Therefore, the mean error across locations is very close to zero. In contrast, the errors in the elevation spectra when using the local depth h_p are primarily positive and tend to increase with increasing frequency (Fig. 12a). The errors for different choices of water depth show that the effective depth correction is able to reduce the overestimates of the observed sea surface elevation spectra. Although site-specific errors after applying the depth corrections can still be fairly large at some locations and frequencies (e.g., see S1 in Fig. 12), note these errors in $\overline{K^2(h_p + \delta h_{\text{bathy}})S_p}$ are usually smaller than errors in $\overline{K^2(h_p)S_p}$ (Fig. 12). A frequency-dependent optimal depth correction $\delta h_{\text{opt}}(f)$ (i.e., by minimizing errors in spectra at each frequency) was considered to reduce site-specific errors. However, $\delta h_{\text{opt}}(f)$ did not have a robust statistical relationship with frequency or with the bathymetry data that could provide a frequency-dependent depth correction.

We next examine the significant wave height errors using the uncorrected ($\delta h = 0$), optimal ($\delta h = \delta h_{\text{opt}}$), and the median depth within $\hat{r} = 13$ m ($\delta h = \delta h_{\text{bathy}}$) at each of the eight locations (Fig. 13). As seen in Fig. 2, the uncorrected error $\epsilon_0^2 = \epsilon^2(0)$ varies by factor of 10, from 110 at S2 to 11 cm^2 at S5 (red bars in Fig. 13). The error with optimal correction $\epsilon^2(\delta h_{\text{opt}})$ (green bars in Fig. 13) is reduced substantially ($>50\%$) relative to ϵ_0^2 at locations with significant ϵ_0^2, such as the S1, S2, S3, S7, and S8 grouping. At locations with weak ϵ_0^2 (S4 and S5), the optimal correction δh_{opt} is small and results in $\epsilon^2(\delta h_{\text{opt}})$ that are similar to ϵ_0^2. Location S8 is an outlier, as $\epsilon^2(\delta h_{\text{bathy}})$ is only slightly reduced from ϵ_0^2. The water depth at S8 is similar to other locations, but the difference between $\overline{h}_p$ and the spatially averaged bathymetry at S8 has a larger magnitude than $\delta h_{\text{opt}} = -0.8$ m (Fig. 9) and is fairly constant with r (Fig. 7a). Therefore, additional metrics of depth variability (e.g., skewness) might need to be considered to reduce H_p^2 errors toward $\epsilon^2(\delta h_{\text{opt}})$. Nevertheless, the correction from the median bathymetry $\epsilon^2(\delta h_{\text{bathy}})$ (blue bar; Fig. 13) tends to be similar to $\epsilon^2(\delta h_{\text{opt}})$ across the eight locations, indicating that using the depth from the averaged bathymetry enables accurate estimation of wave statistics.

5. Discussion

For pressure sensors deployed in bathymetric lows, using linear theory with h_p gives rise to clear errors in significant wave height squared H_p^2 and wave spectra. The agreement between δh_{opt} and δh_{bathy} and the error reduction between ϵ_0^2 and $\epsilon^2(\delta h_{\text{bathy}})$ support the effective depth hypothesis that a water depth from a spatially averaged bathymetry is the appropriate depth to use in linear theory on rough rocky bathymetry with large variability on small spatial scales. We next examine the errors between pressure- and Spotter-based wave statistics relative to a sandy, smooth inner shelf, estimate potential errors in measurements from the coral reef literature, and the implications of an effective depth.

a. *Comparison to a smooth, sandy inner shelf*

Comparisons between collocated pressure sensors and Spotter wave buoys on the inner shelf are not common. In a low-sloped sandy bay in $h \approx 7$-m depth, a pressure sensor integrated within an ADCP had good time-mean sea surface spectra comparison in the sea–swell band to a Spotter wave buoy (Lancaster et al. 2021).

More recently, a range of wave buoys were intercompared to a pressure-sensor array in 8-m water depth on a low-sloped and smooth sandy beach (Collins et al. 2024). The Spotter was deployed 400 m alongshore from the pressure-sensor array over three winter months and the observed H_{sp} varied from 0.5 to 3 m, generally larger than observed here (Fig. 2). In a

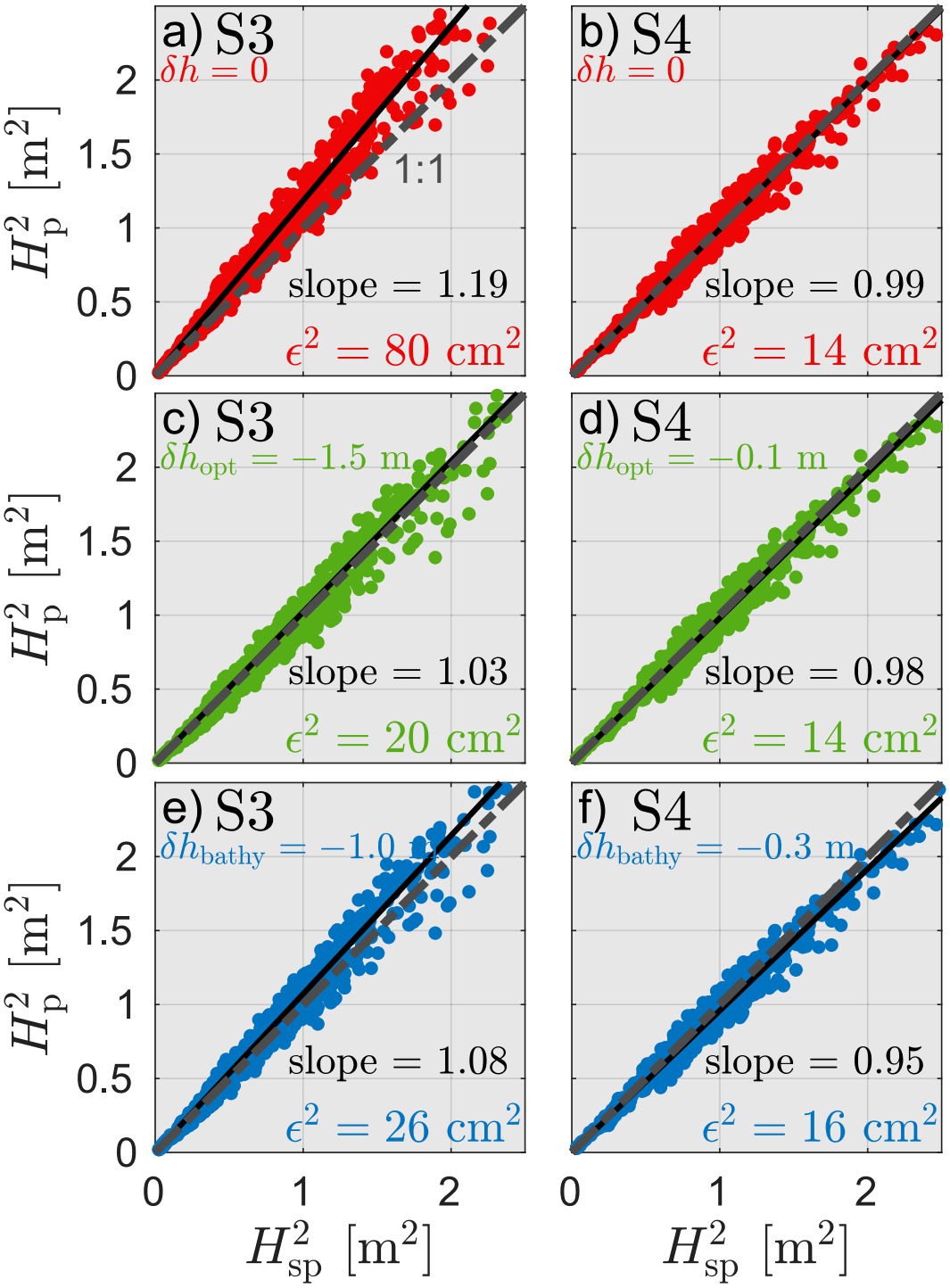

FIG. 10. Collocated hourly pressure-based H_p^2 vs Spotter-based H_{sp}^2 significant wave height squared at locations (a),(c),(e) S3 and (b),(d),(f) S4. For H_p, the transfer function is computed at (a),(b) $\overline{h}_p$, (c),(d) $h_{\mathrm{eff}} = h_p + \delta h_{\mathrm{opt}}$, or (e),(f) $h_{\mathrm{eff}} = h_p + \delta h_{\mathrm{bathy}}$. The bathymetric correction δh, the mean-square error ϵ^2 from (7), and the linear regression slope are shown in each panel. The gray dashed line is the one-to-one line.

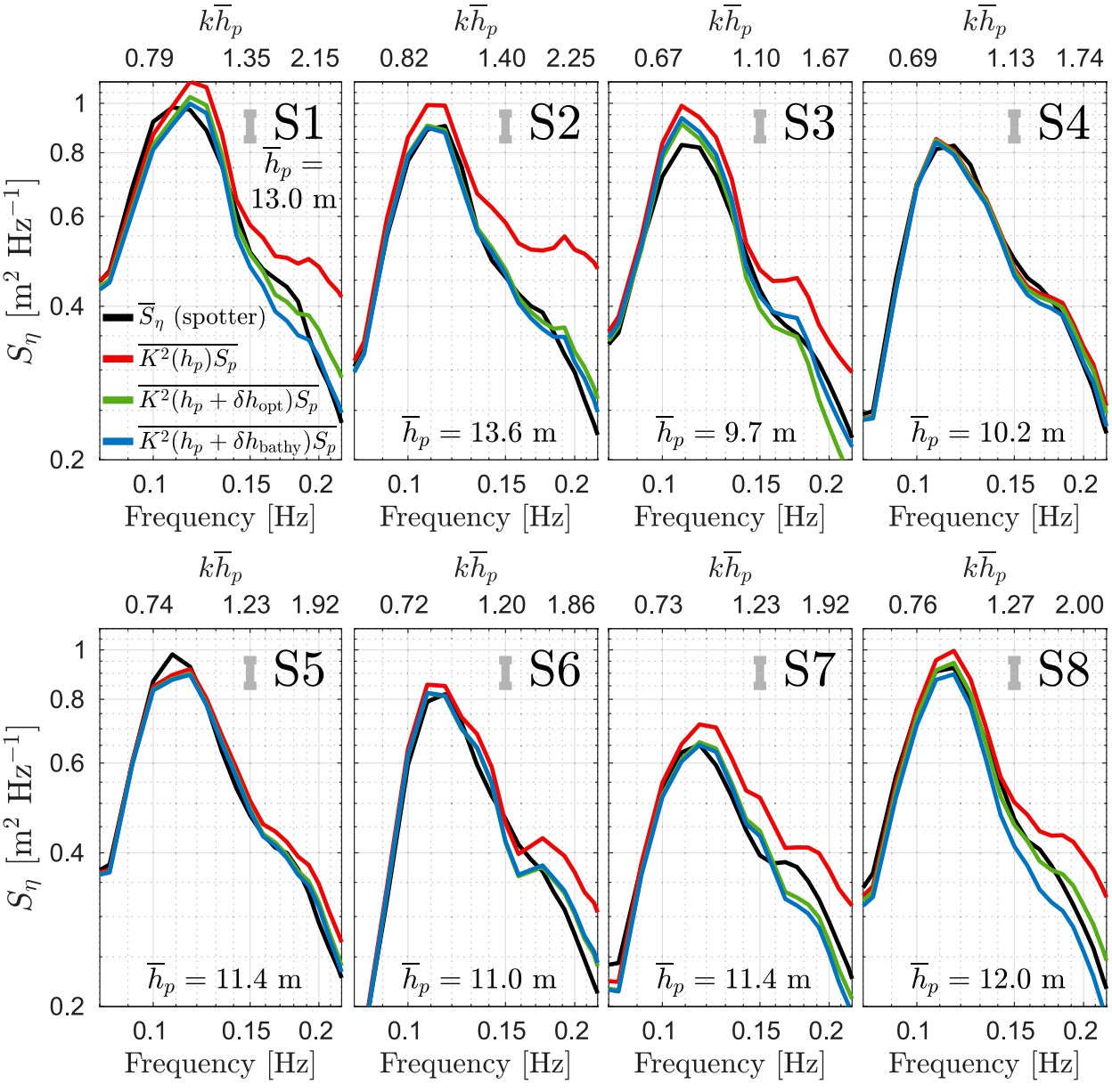

FIG. 11. Time-averaged surface elevation spectra $\overline{S}_\eta$ vs frequency at all Smart Mooring locations. Similar to Fig. 3, the black curve is Spotter-estimated $\overline{S}_\eta$. Three pressure-sensor-estimated spectra are shown: 1) no depth correction [red, $\overline{K^2(h_p)S_p}$], 2) optimal depth correction [green, $\overline{K^2(h_p+\delta h_{\rm opt})S_p}$], and 3) bathymetric correction [blue, $\overline{K^2(h_p+\delta h_{\rm bathy})S_p}$]. Gray bars show the 95% confidence interval. The top axis in each panel shows the nondimensional $k\overline{h}_p$ with $\overline{h}_p$ at each site.

0.1-Hz-wide band spanning similar kh ranges as here, the Collins et al. (2024) ϵ_0^2 from (6) is 36 cm^2, which is partially attributable to process noise (e.g., true alongshore variations in wave height) as the sensors were not collocated. Taking into account processes noise and the larger $H_{\rm sp}$, the Collins et al. (2024) $\epsilon_0^2 = 36\,{\rm cm}^2$ is consistent with the smaller ϵ^2 observed here at locations (S4, S5, S6, and S8) all of which except S8 had small $\delta h_{\rm opt}$ and $\delta h_{\rm bathy}$ (Fig. 9). The locations with ϵ_0^2 much larger than those of Collins et al. (2024) (i.e., S1, S2, S3, and S7) had large $\delta h_{\rm opt}$ and $\delta h_{\rm bathy}$ (with magnitudes > 1 m), and the corrections significantly improved the errors. Therefore, if the standard approach of using h_p to calculate H_p is applied for measurements over rough topography, then the errors can be greater than expected for smooth bathymetry, which corroborates the need for correcting pressure-sensor-based wave statistics.

b. *Application to other regions*

The errors in pressure-based wave measurements observed on rough rocky bathymetry may also occur in other regions with large bathymetric roughness, including coral reefs.

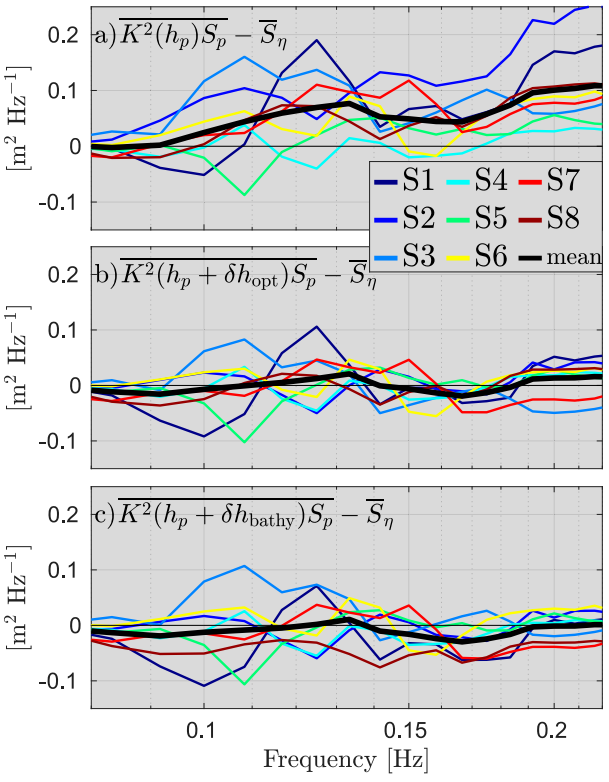

FIG. 12. Errors in time-mean sea surface elevation spectra from pressure sensors $\overline{K^2(h)S_p}$ relative to the Spotter $\overline{S}_\eta$ vs frequency. Transfer functions $K^2(h)$ were evaluated at (a) the local depth h_p, (b) the optimal effective depth $h_p + \delta h_{\rm opt}$, and (c) the effective depth from bathymetry $h_p + \delta h_{\rm bathy}$.

Previous work in these environments has used h_p and flat-bottom linear wave theory to calculate sea–swell wave statistics, but the accuracy of these results has not been addressed. Accurate, high-resolution bathymetry is necessary to address the accuracy of sea–swell wave statistics, but such bathymetry is not always available. The ratio,

$$R \equiv \frac{\cosh^2(k_p h_p)}{\cosh^2(k_{\rm eff} h_{\rm eff})}, \tag{10}$$

provides the overestimate of the wave energy density from a near-bottom pressure sensor in a bathymetric low, where k_p ($k_{\rm eff}$) is the wavenumber calculated through (3) at h_p ($h_{\rm eff}$). For a rough estimate of R, we will approximate the effective depth as $h_{\rm eff} \approx h_p - \sigma_h$, as supported by the correlation of $\delta h_{\rm bathy}$ (or $\delta h_{\rm opt}$) and σ_h, and their similar magnitude (section 4b). Substituting this approximation into (10) yields

$$R \sim \frac{\cosh^2(k_p h_p)}{\cosh^2\left[k_{\rm eff} h_p \left(1 - \frac{\sigma_h}{h_p}\right)\right]}. \tag{11}$$

Small $k_p h_p$ and σ_h/h_p yield negligible errors, indicated by $R \approx 1$, whereas errors grow with increasing $k_p h_p$ or σ_h/h_p (Fig. 14).

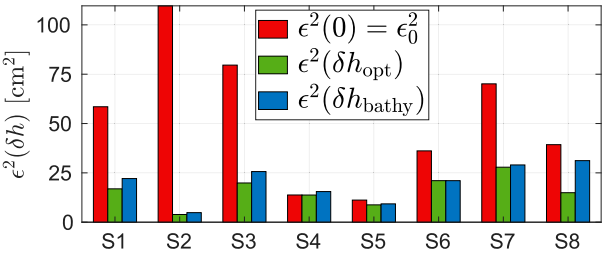

FIG. 13. Mean-square error of H_p^2 relative to $H_{\rm sp}^2$ from (7) using local depth ($\delta h = 0$, red), the optimal depth correction $\delta h_{\rm opt}$ (green), and the correction from the median bathymetry at $\hat{r} = 13$ m $\delta h_{\rm bathy}$ (blue).

In terms of field deployments of pressure sensors, the error R for a wave frequency can be estimated given the standard deviation of water depth and the target depth h_p for the sensor, assumed to be deployed in a bathymetric low. For our Smart Mooring observations at China Rock, σ_h/h_p ranges from 0.07 to 0.1 given $\sigma_h \approx 1$ m within a scale $\hat{r} = 13$ m (Fig. 7b), and pressure sensors deployed at $9.7 \le \bar{h}_p \le 13.6$ m (Fig. 11). The expected R ranges from 1.05 to 1.34 between 0.1 and 0.2 Hz (corresponding to $0.7 < k_p h_p < 2.2$), which indicates that errors in $\overline{K^2(h_p)S_p}$ may be significant, as confirmed by the comparison with the Spotter-based $\overline{S}_\eta$ (Fig. 11). Overall, the analysis of R in (11) suggests that analogous errors to those in this paper may also be present in regions where the bathymetry is particularly rough spanning rocky shorelines to coral reefs.

We now estimate errors based on parameters from previous studies of sea–swell wave transformation over coral reefs. These R are likely overestimates as pressure sensors are assumed to be deployed at the bottom of bathymetric lows. Waves observed on shallow reef flats with $h \approx 1$ m, $\sigma_h \approx 15$ cm, and peak periods from 4 to 8 s (Lentz et al. 2016) result in a 4% overestimate at 4 s. Similar reef flat observations with 10-s peak periods (Sous et al. 2023) lead to negligible error. At greater water depth, errors in wave statistics are potentially larger in observations over reefs at $h \approx 7$ m (Lowe et al. 2005),

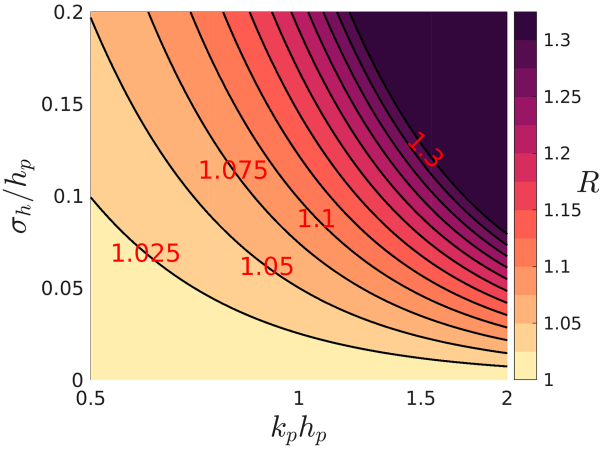

FIG. 14. Estimate of the overprediction of wave energy density R as a function of $k_p h_p$ and σ_h/h_p computed from (11).

although the roughness in this depth was not reported. Over the rougher coral reefs at the Palmyra atoll, with $0.4 \leq \sigma_h \leq 1.3$ m (Monismith et al. 2015; Rogers et al. 2016), observations at $h \approx 11$ m may be as accurate as 2% for low-frequency swell, but overestimates can be as large as 15% for 7-s seas. Even larger depth changes over coral reefs can occur in the presence of spur-and-groove formations. Observations at $h \approx 10$ m of 6-s mean-period waves in 2-m deep, narrow (5 m) grooves (Acevedo-Ramirez et al. 2021) may have large biases of up to 35%. However, these biases may be overestimated given that the dominant wave direction is parallel to the groove and averaging water depth within a radius r of the pressure sensor irrespective of direction may not be appropriate. A further assumption in these R estimates is that wave-induced pressure perturbations over coral reefs have similar characteristics as on rocky bottoms despite likely differences in the submeter roughness morphology or fluid connectivity between the two environments. This assumption needs to be tested for a better quantification of errors in pressure-based sea-swell wave measurements.

c. *Implications of an effective depth*

Although the bathymetric slope at the ROXSI field site is weak ≈0.025 over large scales, the rough rocky bathymetry has large variability, with bottom slopes greater than 0.52 (30°), over short horizontal scales of $O(1)$ m (Fig. 1). Nevertheless, surface gravity waves propagate coherently over rough rocky bathymetry as if there is a dispersion relationship with an effective depth that is some spatial average of the bathymetry they are propagating over. For pressure sensors in bathymetric lows in 10–13-m water depth, we found an averaging length scale of $\hat{r} = 13$ m led to the smallest error in the 0.1–0.2-Hz band (Fig. 9). However, the estimated $\hat{r}$ is limited by the water depth of the Smart Mooring sites and the wave periods in the ROXSI experiment, and thus, the appropriate averaging scale at other depths and/or wave conditions is unclear. Via dimensional reasoning, we argue that the relevant nondimensional parameter is the ratio of the averaging scale to the wavelength $\hat{r}/\lambda$.

For our Smart Mooring measurements, H_p was calculated within the 0.1–0.2-Hz frequency band. Since the errors in the sea surface elevation spectrum increase with frequency, we take λ at 0.2 Hz, and with $h = 10$ m, $\hat{r}/\lambda = 13/37 \approx 0.36$. A bathymetry averaging radius can be calculated at other water depths by taking a constant $\hat{r}/\lambda = 0.36$ and computing the wavelength at 0.2 Hz from the dispersion relationship (3). The term $\hat{r}$ gets shorter (longer) as the water depth decreases (increases), such that $\hat{r} \approx 7.5$ m at a water depth of 2 m. Since errors in pressure-based S_η are small for $kh < 0.7$ and the transfer function is less sensitive to the choice of water depth, errors in S_η at $f = 0.11$ Hz should be small in water depths shallower than 8 m. Nevertheless, errors in S_η at 0.2 Hz can still be significant in water depths around 2 m and averaging the bathymetry is important for correcting S_η at these higher frequencies.

Our results imply that the bed is effectively at $z = -h_{\text{eff}}$ for the dispersion relationship (3) and the transfer function (2) and that the wave pressure signal does not decay in the vertical for $-h_p \leq z \leq -h_{\text{eff}}$. We hypothesize that horizontal orbital velocities are largely constrained to be zero within narrow bathymetric lows relative to the wavelength, and through the Bernoulli equation, the wave-induced pressure is hydrostatic due to a time-varying, spatially uniform velocity potential. In this scenario, the wave-induced pressure spectrum is vertically uniform within the bathymetric low. This vertically homogeneous vertical profile is qualitatively different than the frequency-dependent attenuation of the wave-induced pressure in interstitial sand pores (Raubenheimer et al. 1998). Within saturated sand, Raubenheimer et al. (1998) showed that a frequency-dependent transfer function can convert the measured buried pressure spectra to that at the top of the seabed, after which (2) is used to calculate the sea surface elevation spectra. In contrast, the proposed effective depth hypothesis only includes a depth correction δh to the transfer function (2) from pressure to sea surface elevation spectra. The morphology of the roughness, potentially reflected by higher-order moments such as skewness, could also then affect the vertical structure of wave pressure within bathymetric depressions.

Our effective depth correction is a simple method that reduces errors in pressure-based wave statistics. Further research on the near-bed fluid dynamics of waves propagating over rough bathymetry is required to potentially derive additional corrections. The fluid dynamics of orbital velocities and pressure near the bottom of rough rocky bathymetry is largely unstudied, and no theory exists linear or otherwise. Over random bathymetry, a high-resolution [e.g., LES or direct numerical simulation (DNS)] numerical model is required to resolve the spatiotemporal variability of near-bottom pressure due to surface gravity waves. Such modeling would allow the development of a more comprehensive bathymetric correction δh_{bathy} that could potentially include multiple statistical moments of the bathymetry. Further work on detailed near-bottom wave dynamics over rough rocky bathymetry is forthcoming.

Future pressure-sensor deployments can benefit from high-resolution bathymetry to inform decisions on instrument location, estimate errors in surface wave observations, and correct wave statistics with an effective depth. High-resolution bathymetry is important for planning instrument deployment over rough seabeds given the inherently large water depth variability. For example, bathymetry data provide σ_h, and thus, significant wave height error estimates R through (11). If σ_h and R are spatially variable, then regions with smaller seabed roughness could be targeted for pressure-sensor deployment and thereby reduce observational errors. For increasing roughness (σ_h and R), the effective depth correction becomes more important for estimating accurate sea–swell wave statistics. To estimate gradients of wave energy fluxes, errors can arise if sensors are too closely separated, where apparent changes in energy flux can overwhelm small actual energy flux differences. Therefore, pressure sensors should be deployed with sufficient separation such that the expected actual changes in energy flux are significantly larger than potential errors from R. Along with high-resolution bathymetry, the

deployment of pressure sensors also benefits from scuba diving capabilities. For the ROXSI observations, divers determined the exact deployment location on site to minimize the likelihood of instruments moving during the experiment. Local bathymetric lows were the most appropriate choice. Given different instrument platforms, seabed morphology, or scientific goals, other choices for deploying pressure sensors on rough seabeds could be considered.

6. Summary

We present surface gravity wave observations from eight collocated bottom-mounted pressure sensors and Spotter wave buoys in 10–13-m water depth from the 5-week ROXSI field experiment, at a site with rough rocky bathymetry on the Monterey Peninsula. The rough bathymetry has large $O(1)$ m vertical variability on $O(1–10)$ m horizontal scales. Pressure sensors were deployed by divers in rocky bathymetric lows to enhance sensor stability in large waves. Using the pressure-sensor-estimated water depth h_p, the pressure-based significant wave height squared consistently overestimates wave buoy measurements (as large as 21%). Some locations have large mean-square error ϵ_0^2 between pressure- and buoy-based wave height, where ϵ_0^2 is 1.5–3 larger than in wave buoy measurements on a sandy, low-sloped inner shelf (Collins et al. 2024). The time-mean pressure-sensor-based wave spectra are elevated in the sea band (0.1–0.2 Hz) relative to the Spotter. These errors are consistent with the depth h_p being too large when evaluating the linear-theory-based transfer function (2). An effective depth hypothesis is proposed, where a depth based on the spatially averaged bathymetry is more appropriate than h_p to use with linear theory for estimating wave statistics from pressure observations. This hypothesis is consistent with an assumption that an approximately linear wave field is not strongly modified by abrupt changes in water depth (i.e., $\sigma_h \sim 1$ m and $\sigma_h/h \sim 0.1$) over horizontal scales of $O(1–10)$ m. An optimal depth correction δh_{opt} is estimated by minimizing the error between significant wave heights from pressure sensors and Spotter wave buoys. The optimal correction to the local depth is $-1.6 \leq \delta h_{\text{opt}} < -0.1$ m across the eight locations, where the sign is consistent with pressure sensors in bathymetric lows and an effective depth shallower than h_p. A bathymetry averaging scale of $\hat{r} = 13$ m is found by minimizing the squared difference between the correction from the median bathymetry and the optimal depth correction. The optimal and averaged bathymetry depth corrections are similar across locations. Both corrections, using linear theory, significantly improve errors in wave statistics, particularly in locations with large δh_{bathy} and large errors ϵ_0^2. The reduced errors suggest that linear wave theory provides a reasonable framework to study sea–swell wave transformation despite the complex bathymetry, but a spatially averaged bathymetry needs to be taken into account. Therefore, accurate, high-resolution bathymetry, with at least $O(1)$ m resolution, is necessary to calculate the spatially averaged depth around a pressure sensor and improve estimates of wave statistics. For application to other depths or frequencies, we argue that the ratio of the averaging scale to the wavelength at the upper-frequency bound for significant wave height should be kept constant. The expected errors R in the surface elevation spectrum can be calculated from (11), and R increases with σ_h/h and kh. While approximately shallow water waves over shallow coral reefs have negligible errors, measurements at deeper water in rough coral reefs may have pressure-based wave statistics with similar errors to our observations on rocky bathymetry.

Acknowledgments. This paper is part of the Rocky Shores Experiments and Simulations (ROXSI), with funding by the Office of Naval Research through grants N000142112786 and N0001423WX01357. The Monterey NOAA Sanctuary, California Fish and Wildlife, Pebble Beach, and Pacific Grove provided environmental permission for the experiment, and we thank Chris Miller for support with the permitting process. We thank the SIO and NPS field crews for their invaluable support with the field experiment; for SIO, Brian Woodward, Kent Smith, Rob Grenzeback, Lucian Parry, Shane Finnerty, Carson Black, Duncan Wheeler, Annie Adelson, Loren Clark, Kaden Quinn, and Kanoa Pick; and for NPS, Ed Thornton, Paul Jessen, Charlotte Benbow, Pat Collins, Mike Cook, Matt Gough, and Ian Jenstrom. We appreciate the valuable discussions with the ROXSI team (Johanna Rosman, Greg Wilson, Ata Suanda, Mika Malila, Matt Conlin, and César Acevedo-Ramirez) that informed this manuscript. We appreciate the comments from the reviewers, which helped to improve this manuscript.

Data availability statement. The data presented in this paper have been archived in a Zenodo repository and are available at https://doi.org/10.5281/zenodo.13242438. Source code for data processing and generating figures is available at the GitHub repository github.com/olavobm/Paper_EffectiveDepth.

REFERENCES

Acevedo-Ramirez, C. A., W. Stephenson, S. Wakes, and I. Mariño-Tapia, 2021: Wave transformation on a fringing reef system with spur and groove structures. *J. Geophys. Res. Oceans*, **126**, e2020JC016910, https://doi.org/10.1029/2020JC016910.

Barnard, P. L., L. H. Erikson, and R. G. Kvitek, 2011: Small-scale sediment transport patterns and bedform morphodynamics: New insights from high-resolution multibeam bathymetry. *Geo-Mar. Lett.*, **31**, 227–236, https://doi.org/10.1007/s00367-011-0227-1.

Beckman, J. N., and J. W. Long, 2022: Quantifying errors in wind and wave measurements from a compact, low-cost wave buoy. *Front. Mar. Sci.*, **9**, 966855, https://doi.org/10.3389/fmars.2022.966855.

Bertin, X., and Coauthors, 2018: Infragravity waves: From driving mechanisms to impacts. *Earth-Sci. Rev.*, **177**, 774–799, https://doi.org/10.1016/j.earscirev.2018.01.002.

Bishop, C. T., and M. A. Donelan, 1987: Measuring waves with pressure transducers. *Coastal Eng.*, **11**, 309–328, https://doi.org/10.1016/0378-3839(87)90031-7.

Bonneton, P., and D. Lannes, 2017: Recovering water wave elevation from pressure measurements. *J. Fluid Mech.*, **833**, 399–429, https://doi.org/10.1017/jfm.2017.666.

——, ——, K. Martins, and H. Michallet, 2018: A nonlinear weakly dispersive method for recovering the elevation of irrotational surface waves from pressure measurements. *Coastal Eng.*, **138**, 1–8, https://doi.org/10.1016/j.coastaleng.2018.04.005.

Collins, C. O., and Coauthors, 2024: Performance of moored GPS wave buoys. *Coastal Eng. J.*, **66**, 17–43, https://doi.org/10.1080/21664250.2023.2295105.

CSUMB, Seafloor Mapping Laboratory, 2014: California Seafloor Mapping Project – Undersea Imagery Archive 2007–2014. https://csumb.edu/undersea/seafloor-maps.

Davis, K. A., G. Pawlak, and S. G. Monismith, 2021: Turbulence and coral reefs. *Annu. Rev. Mar. Sci.*, **13**, 343–373, https://doi.org/10.1146/annurev-marine-042120-071823.

Dean, R. G., and R. A. Dalrymple, 1991: *Water Wave Mechanics for Engineers and Scientists*. Advanced Series on Ocean Engineering, Vol. 2, World Scientific Publishing Company, 368 pp.

Elfrink, B., and T. Baldock, 2002: Hydrodynamics and sediment transport in the swash zone: A review and perspectives. *Coastal Eng.*, **45**, 149–167, https://doi.org/10.1016/S0378-3839(02)00032-7.

Elgar, S., B. Raubenheimer, and R. T. Guza, 2001: Current meter performance in the surf zone. *J. Atmos. Oceanic Technol.*, **18**, 1735–1746, https://doi.org/10.1175/1520-0426(2001)018<1735:CMPITS>2.0.CO;2.

Farrell, E. J., H. Granja, L. Cappietti, J. T. Ellis, B. Li, and D. J. Sherman, 2009: Wave transformation across a rock platform, Belinho, Portugal. *J. Coastal Res.*, **1**, 44–48.

Gomes da Silva, P., G. Coco, R. Garnier, and A. H. F. Klein, 2020: On the prediction of runup, setup and swash on beaches. *Earth-Sci. Rev.*, **204**, 103148, https://doi.org/10.1016/j.earscirev.2020.103148.

Gon, C. J., J. H. MacMahan, E. B. Thornton, and M. Denny, 2020: Wave dissipation by bottom friction on the inner shelf of a rocky shore. *J. Geophys. Res. Oceans*, **125**, e2019JC015963, https://doi.org/10.1029/2019JC015963.

Guza, R. T., and E. B. Thornton, 1980: Local and shoaled comparisons of sea surface elevations, pressures, and velocities. *J. Geophys. Res.*, **85**, 1524–1530, https://doi.org/10.1029/JC085iC03p01524.

Hasselmann, K., 1962: On the non-linear energy transfer in a gravity-wave spectrum Part 1. General theory. *J. Fluid Mech.*, **12**, 481–500, https://doi.org/10.1017/S0022112062000373.

Herbers, T. H. C., R. L. Lowe, and R. T. Guza, 1992: Field observations of orbital velocities and pressure in weakly nonlinear surface gravity waves. *J. Fluid Mech.*, **245**, 413–435, https://doi.org/10.1017/S0022112092000521.

——, S. Elgar, and R. T. Guza, 1999: Directional spreading of waves in the nearshore. *J. Geophys. Res.*, **104**, 7683–7693, https://doi.org/10.1029/1998JC900092.

——, ——, N. A. Sarap, and R. T. Guza, 2002: Nonlinear dispersion of surface gravity waves in shallow water. *J. Phys. Oceanogr.*, **32**, 1181–1193, https://doi.org/10.1175/1520-0485(2002)032<1181:NDOSGW>2.0.CO;2.

——, P. F. Jessen, T. T. Janssen, D. B. Colbert, and J. H. MacMahan, 2012: Observing ocean surface waves with GPS-tracked buoys. *J. Atmos. Oceanic Technol.*, **29**, 944–959, https://doi.org/10.1175/JTECH-D-11-00128.1.

Lancaster, O., R. Cossu, S. Boulay, S. Hunter, and T. E. Baldock, 2021: Comparative wave measurements at a wave energy site with a recently developed low-cost wave buoy (Spotter), ADCP, and pressure loggers. *J. Atmos. Oceanic Technol.*, **38**, 1019–1033, https://doi.org/10.1175/JTECH-D-20-0168.1.

Lavaud, L., X. Bertin, K. Martins, M. Pezerat, T. Coulombier, and D. Dausse, 2022: Wave dissipation and mean circulation on a shore platform under storm wave conditions. *J. Geophys. Res. Earth Surf.*, **127**, e2021JF006466, https://doi.org/10.1029/2021JF006466.

Lentz, S., and B. Raubenheimer, 1999: Field observations of wave setup. *J. Geophys. Res.*, **104**, 25 867–25 875, https://doi.org/10.1029/1999JC900239.

Lentz, S. J., J. H. Churchill, K. A. Davis, and J. T. Farrar, 2016: Surface gravity wave transformation across a platform coral reef in the Red Sea. *J. Geophys. Res. Oceans*, **121**, 693–705, https://doi.org/10.1002/2015JC011142.

Lowe, R. J., J. L. Falter, M. D. Bandet, G. Pawlak, M. J. Atkinson, S. G. Monismith, and J. R. Koseff, 2005: Spectral wave dissipation over a barrier reef. *J. Geophys. Res.*, **110**, C04001, https://doi.org/10.1029/2004JC002711.

MacMahan, J., Ed B. Thornton, and Ad J. H. M. Reniers, 2006: Rip current review. *Coastal Eng.*, **53**, 191–208, https://doi.org/10.1016/j.coastaleng.2005.10.009.

Martins, K., P. Bonneton, D. Lannes, and H. Michallet, 2021: Relation between orbital velocities, pressure, and surface elevation in nonlinear nearshore water waves. *J. Phys. Oceanogr.*, **51**, 3539–3556, https://doi.org/10.1175/JPO-D-21-0061.1.

Monismith, S. G., 2007: Hydrodynamics of coral reefs. *Annu. Rev. Fluid Mech.*, **39**, 37–55, https://doi.org/10.1146/annurev.fluid.38.050304.092125.

——, J. S. Rogers, D. Koweek, and R. B. Dunbar, 2015: Frictional wave dissipation on a remarkably rough reef. *Geophys. Res. Lett.*, **42**, 4063–4071, https://doi.org/10.1002/2015GL063804.

Moulton, M., S. H. Suanda, J. C. Garwood, N. Kumar, M. R. Fewings, and J. M. Pringle, 2023: Exchange of plankton, pollutants, and particles across the nearshore region. *Annu. Rev. Mar. Sci.*, **15**, 167–202, https://doi.org/10.1146/annurev-marine-032122-115057.

OCM Partners, 2024: 2013 NOAA Coastal California Topobathy Merge Project. NOAA Office for Coastal Management, accessed 19 May 2024, https://www.fisheries.noaa.gov/inport/item/49649.

Poate, T., G. Masselink, M. J. Austin, M. Dickson, and R. McCall, 2018: The role of bed roughness in wave transformation across sloping rock shore platforms. *J. Geophys. Res. Earth Surf.*, **123**, 97–123, https://doi.org/10.1002/2017JF004277.

Raghukumar, K., G. Chang, F. Spada, C. Jones, T. Janssen, and A. Gans, 2019: Performance characteristics of "Spotter," a newly developed real-time wave measurement buoy. *J. Atmos. Oceanic Technol.*, **36**, 1127–1141, https://doi.org/10.1175/JTECH-D-18-0151.1.

Raubenheimer, B., R. T. Guza, and S. Elgar, 1996: Wave transformation across the inner surf zone. *J. Geophys. Res.*, **101**, 25 589–25 597, https://doi.org/10.1029/96JC02433.

——, S. Elgar, and R. T. Guza, 1998: Estimating wave heights from pressure measured in sand bed. *J. Waterw. Port Coastal Ocean Eng.*, **124**, 151–154, https://doi.org/10.1061/(ASCE)0733-950X(1998)124:3(151).

——, R. T. Guza, and S. Elgar, 2001: Field observations of wave-driven setdown and setup. *J. Geophys. Res.*, **106**, 4629–4638, https://doi.org/10.1029/2000JC000572.

Rogers, J. S., S. G. Monismith, D. A. Koweek, and R. B. Dunbar, 2016: Wave dynamics of a Pacific Atoll with high frictional effects. *J. Geophys. Res. Oceans*, **121**, 350–367, https://doi.org/10.1002/2015JC011170.

Sofar Ocean, 2024: Sofar Ocean. Accessed 19 May 2024, https://www.sofarocean.com/products/spotter#s-key.

Sous, D., K. Martins, M. Tissier, F. Bouchette, and S. Meule, 2023: Spectral wave dissipation over a roughness-varying barrier reef. *Geophys. Res. Lett.*, **50**, e2022GL102104, https://doi.org/10.1029/2022GL102104.

Thornton, E. B., and R. T. Guza, 1982: Energy saturation and phase speeds measured on a natural beach. *J. Geophys. Res.*, **87**, 9499–9508, https://doi.org/10.1029/JC087iC12p09499.

——, and ——, 1983: Transformation of wave height distribution. *J. Geophys. Res.*, **88**, 5925–5938, https://doi.org/10.1029/JC088iC10p05925.